Available online at www.sciencedirect.com

SciVerse ScienceDirect

Procedia Computer Science 18 (2013) 1068 – 1076

Procedia Computer Science

International Conference on Computational Science, ICCS 2013

Isogeometric Analysis of Coupled Thermo-Mechanical Phase-Field Models for Shape Memory Alloys Using Distributed Computing

R. Dhote[a,c], H. Gomez[b], R. Melnik[c], J. Zu[a]

[a]*Department of Mechanical and Industrial Engineering, University of Toronto, 5 King's College Road, Toronto, ON, M5S3G8, Canada*
[b]*Department of Applied Mathematics, University of A Coruña, Spain*
[c]*M²NeT Laboratory, Wilfrid Laurier University, Waterloo, ON, N2L3C5, Canada*

Abstract

A variational formulation and numerical implementation of the phase-field models for shape memory alloys using distributed computing are reported in the paper. The numerical implementation is based on the isogeometric analysis framework, constituting the rich NURBS basis functions. The phase field models are developed using the strain based order parameter and the Ginzburg-Landau theory. The fourth order fully coupled thermo-mechanical 2D and 3D models are solved with the isogeometric finite element methodology in the distributed computing environment. The weak scaling performance studies on the 2D model demonstrate current challenges and open a way for future improvements.

Keywords: Isogeometric analysis ; martensitic transformations ; phase-field model; Ginzburg-Landau theory; nonlinear thermo-elasticity; distributed computing

1. Introduction

Shape memory alloys (SMAs) are a prime example of materials exhibiting multiscale and multiphysics behaviors. Upon thermal and mechanical loadings, the atoms rearrange from a highly symmetric crystal lattice to its lower symmetric counterpart, giving rise to macroscale phenomena like shape memory effect and superelasticity. Although the first SMA material was discovered in 1932 (by Ölander in Au-Cd alloy [1]), up until today their mathematical modeling remains a challenging task in science and engineering. The main reasons behind that are the inherent coupling between thermal and mechanical (structural) physics and the martensitic phase transformations. Coupling effects are difficult to treat numerically and the resulting complex problem is often reduced to a simple formulation, at the expense of details leading to physical considerations away from reality.

Several modeling approaches have been developed over the last years to capture the behavior of SMAs observed experimentally. Extensive discussions of corresponding models are given in the review papers [2, 3, 4].

*Rakesh Dhote. Tel.: +1-416-946-3709 ; fax: +1-416-978-7753.
E-mail address: rakesh.dhote@mail.utoronto.ca.

Selection and peer review under responsibility of the organizers of the 2013 International Conference on Computational Science
doi:10.1016/j.procs.2013.05.272

Specifically, the phase-field (PF) models are of particular interest here. The PF models provide a unified framework that can describe stress and temperature induced phase transformations, including their dynamics, in the variational settings. These models have been used to study microstructures and mechanical properties of SMAs across different length scales [5, 6, 7, 8, 9, 10, 11]. We have developed the 2D and 3D models with main focus on capturing the thermo-mechanical coupling in SMAs, which has been treated predominantly under isothermal assumptions in the literature [8, 9].

The strain based PF model formulation leads to fourth-order partial differential equations (PDEs) in space by introducing a smoothly varying interface between different phases in a domain. Numerical methodologies such as finite difference, finite volume, and spectral methods have been traditionally used in this field for solving higher order PDEs [9, 12]. These methodologies have been mostly applied to simple geometries. However, for the real world SMA applications [1], a more geometrically flexible technology needs to be utilized. A finite element method (FEM) is an effective choice to meet this requirement. In the literature, the FEM has been used to solve the second order PDEs, where the continuity requirements on the trial functions can be reduced to global $\mathscr{C}^0$-continuity. For the fourth-order PDEs, the basis functions need to be piecewise smooth and globally $\mathscr{C}^1$-continuous [13]. The finite elements constructed from the class of global $\mathscr{C}^1$-continuous basis functions are referred as $\mathscr{C}^1$-elements. There are limited finite elements which possess $\mathscr{C}^1$-continuity on complex geometries [14]. Recently, Hughes et al. [13] introduced a new finite element methodology known as the isogeometric analysis (IGA). IGA employs the complex non-uniform rational B-spline (NURBS) based geometry in a finite element analysis application directly. IGA offers unique advantages in solving problems involving higher-order PDEs such as higher order accuracy, robustness, two- and three- dimensional geometric flexibility, compact support, and $\mathscr{C}^1$ or higher-order continuity. The IGA methodology has been successfully applied to obtain the solutions to a number of important problems (e.g. the higher-order PDEs in [15, 14], among others). In this paper, we propose the IGA method to solve the developed 2D and 3D phase-field models. To the best of our knowledge, we are using the IGA method for the first time to solve the 3D PF models for SMAs. These models are too complex (having highly nonlinear hysteretic behavior [16], strong thermo-mechanical coupling, and fourth-order differential terms in a space), to solve on a regular workstation. We use the distributed computing environment for the numerical solutions.

In the following sections, we first describe the development of phase-field models based on the non-convex free energy functional, followed by the numerical implementation using isogeometric analysis. Later, the numerical experiments using the developed models in the distributed computing environment are described followed by the simulation results.

2. Phase-Field Models of SMA Dynamics

The SMAs have temperature dependent microstructure phases. The material exists in the symmetric phase (austenite) above the transition temperature θ_m and low temperature phases (martensites) below θ_m. This behavior can be described by using the Landau theory of phase-transformations in terms of polynomial expansion of order parameter (OP; OP is introduced to distinguish different phases in a domain) expressed as the non-convex free energy functional. The minima of the free energy correspond to stable or meta-stable phases in SMAs. The domain wall between martensites is introduced via the Ginzburg term. A generalized form of the free energy functional $\mathscr{F}$ is written as

$$\mathscr{F} = \mathscr{F}_{\text{nop}} + \mathscr{F}_{\text{op}} + \mathscr{F}_{\text{gradient}}, \tag{1}$$

where $\mathscr{F}_{\text{op}}$ is the energy part due to the OPs, which contributes to MT as per the Landau-Devonshire theory, $\mathscr{F}_{\text{nop}}$ is the energy part due to the elastic energy, and $\mathscr{F}_{\text{gradient}}$ is the gradient energy which contributes to the energy cost required for maintaining different phase domains in a structure and interface formed between physical boundaries and domain. The gradient energy term (or the Ginzburg energy) maintains a non-zero width in austenite-martensite and martensite-martensite interfaces, and prevents the system from creating an infinite number of interfaces [17]. The free energy functional components of the 2D model are

$$\begin{aligned}
\mathscr{F}_{nop_{2D}} &= \frac{a_{21}}{2}e_1^2 + \frac{a_{23}}{2}e_6^2, \\
\mathscr{F}_{op_{2D}} &= \frac{a_{22}}{2}\tau e_2^2 - \frac{a_{24}}{4}e_2^4 + \frac{a_{26}}{6}e_2^6, \\
\mathscr{F}_{gradient_{2D}} &= \frac{k_g}{2}\nabla e_2^2,
\end{aligned} \tag{2}$$

and for the 3D model they are

$$\begin{aligned}
\mathscr{F}_{nop_{3D}} &= \frac{a_{31}}{2}\left[e_1 - E_0(e_2^2 + e_3^2)\right]^2 + \frac{a_{36}}{2}\left[e_4^2 + e_5^2 + e_6^2\right], \\
\mathscr{F}_{op_{3D}} &= \frac{a_{32}}{2}\tau(e_2^2 + e_3^2) + \frac{a_{33}}{2}e_3(e_3^2 - 3e_2^2) + \frac{a_{34}}{2}(e_2^2 + e_3^2)^2, \\
\mathscr{F}_{gradient_{3D}} &= \frac{k_g}{2}\left[(\nabla e_2)^2 + (\nabla e_3)^2\right],
\end{aligned} \tag{3}$$

where a_{ij}, E_0, k_g are the material parameters and τ is the rescaled temperature coefficient as a function of transition temperature θ_m. The e_i are the strain components following the Voigt's notation defined using the Cauchy-Lagrange strain tensor $\mathbf{e}$ with $e_{ij} = \left[\left(\partial u_i/\partial x_j\right) + \left(\partial u_j/\partial x_i\right)\right]/2$ (using the repeated index convention) and $\mathbf{u} = \{u_i\}|_{i=1,2,3}$ are the displacements along x, y, and z direction, respectively. The dissipational functional $\mathscr{R}$ is defined as

$$\mathscr{R} = \frac{\eta}{2}\sum_{i=1}^{n}\dot{e}_i^2, \tag{4}$$

where η is the dissipation coefficient.

The coupled equations of dynamic thermoelasticity are derived following the governing equations of momentum and internal energy [11] as

$$\dot{\mathbf{u}} = \mathbf{v}, \tag{5}$$

$$\rho\dot{\mathbf{v}} = \nabla\cdot\boldsymbol{\sigma} + \nabla\cdot\boldsymbol{\sigma}' + \boldsymbol{\sigma}_g + \mathbf{f}, \tag{6}$$

$$\rho\dot{e} - \boldsymbol{\sigma}^T : (\nabla\mathbf{v}) + \nabla\cdot\mathbf{q} = g, \tag{7}$$

where ρ is the mass density, $\boldsymbol{f}$, and g are the mechanical and thermal loadings. The stress tensors $\boldsymbol{\sigma}$, dissipational stress tensors $\boldsymbol{\sigma}'$, and gradient components of stress $\boldsymbol{\sigma}_g$ are defined as

$$\boldsymbol{\sigma} = \frac{\partial}{\partial e_{ij}}\left(\mathscr{F}_{nop} + \mathscr{F}_{op}\right), \qquad \boldsymbol{\sigma}' = \frac{\partial\mathscr{R}}{\partial\dot{e}_{ij}}, \qquad \boldsymbol{\sigma}_g = \frac{\partial}{\partial e_{ij}}\left(\mathscr{F}_{gradient}\right). \tag{8}$$

The two-way thermo-mechanical coupling is established between equations (5)-(7) via temperature θ, strain, and strain rate. We convert the governing equations into the non-dimensional form and solve them numerically using isogeometric analysis.

3. Isogeometric Analysis

We first convert the system of the governing equations into the weak formulation. The domain is discretized using $\mathscr{C}^1$-continuous functions required for the fourth-order PDEs [13, 15]. The generalized-α method is used for time integration along with an adaptive time stepping scheme developed by the authors of [15].

3.1. Weak Formulation

Let $\Omega \subset \mathbb{R}^d$ be an open set in the d-dimensional space (d = 2,3). The boundary is denoted by Γ and its outward normal by $\boldsymbol{n}$. The weak formulation of Eqs. (5)-(7) is derived by multiplying the equations with weighing functions $\{\boldsymbol{U}, \boldsymbol{V}, \Theta\}$ and transforming them by using the integration by parts. Let X denote both the trial solution and weighting function spaces, which are assumed to be identical. Initially, we consider periodic boundary conditions in all directions. Let $(\cdot,\cdot)_\Omega$ denote the L^2 inner product with respect to the domain Ω. The variational formulation is stated as follows:
Find solution $\boldsymbol{S} = \{\boldsymbol{u}, \boldsymbol{v}, \theta\} \in X$ such that $\forall \boldsymbol{W} = \{\boldsymbol{U}, \boldsymbol{V}, \Theta\} \in X$:

$$B(\boldsymbol{W}, \boldsymbol{S}) = 0, \tag{9}$$

with

$$\begin{aligned} B(\boldsymbol{W}, \boldsymbol{S}) \quad = \quad & \left(\boldsymbol{U}, \frac{\partial \boldsymbol{u}}{\partial t}\right)_\Omega + \left(\boldsymbol{V}, \rho \frac{\partial \boldsymbol{v}}{\partial t}\right)_\Omega + \left(\Theta, c_v \frac{\partial \theta}{\partial t}\right)_\Omega - (\boldsymbol{U}, \boldsymbol{v})_\Omega \\ & + (\nabla \boldsymbol{V}, \boldsymbol{\sigma})_\Omega + (\nabla \boldsymbol{V}, \eta \boldsymbol{v})_\Omega - (\boldsymbol{V}, \boldsymbol{f})_\Omega + \left(\boldsymbol{V}, \boldsymbol{\sigma}_g\right)_\Omega \\ & + (\nabla \Theta, \kappa \nabla \theta)_\Omega - (\Theta, g)_\Omega - (\chi_d)_\Omega \,, \end{aligned} \tag{10}$$

where c_v, κ are the material constants, and the weak coupling terms $(\chi_d)_\Omega$ for the d-dimensional space are defined as

$$(\chi_2)_\Omega \quad = \left(\Theta, a_2 \frac{\theta}{\theta_m} e_2 \frac{\partial e_2}{\partial t}\right), \tag{11}$$

$$\begin{aligned} (\chi_3)_\Omega \quad = & \left(\Theta, \Xi\theta \left[\frac{\partial v_1}{\partial x}\left(\frac{\partial u_2}{\partial y} + \frac{\partial u_3}{\partial z} - 2\frac{\partial u_1}{\partial x}\right) + \frac{\partial v_2}{\partial y}\left(\frac{\partial u_1}{\partial x} + \frac{\partial u_3}{\partial z} - 2\frac{\partial u_2}{\partial y}\right)\right.\right. \\ & \left.\left. + \frac{\partial v_3}{\partial z}\left(\frac{\partial u_1}{\partial x} + \frac{\partial u_2}{\partial y} - 2\frac{\partial u_3}{\partial z}\right)\right]\right), \end{aligned} \tag{12}$$

where a_2 and Ξ are the constants.

3.2. Semi-Discrete Formulation

The semi-discrete formulation is used for solving the coupled dynamic thermo-mechanical Eqs. (9). The space is discretized using the Galerkin finite element scheme and time is treated as continuous. We approximate Eqs. (9) by the following variational problem over the finite element spaces (denoted by superscript h):
Find $\boldsymbol{S}^h = \{\boldsymbol{u}^h, \boldsymbol{v}^h, \theta^h\} \in X^h \subset X$ such that $\forall \boldsymbol{W}^h = \{\boldsymbol{U}^h, \boldsymbol{V}^h, \Theta^h\} \in X^h \subset X$:

$$B(\boldsymbol{W}^h, \boldsymbol{S}^h) = 0, \tag{13}$$

with $\boldsymbol{W}^h$ and $\boldsymbol{S}^h$ defined as

$$\boldsymbol{W}^h = \{\boldsymbol{U}^h, \boldsymbol{V}^h, \Theta^h\}, \qquad \boldsymbol{U}^h = \sum_{A=1}^{n_b} \boldsymbol{U}_A N_A, \qquad \boldsymbol{V}^h = \sum_{A=1}^{n_b} \boldsymbol{V}_A N_A, \qquad \Theta^h = \sum_{A=1}^{n_b} \Theta_A N_A, \tag{14}$$

$$\boldsymbol{S}^h = \{\boldsymbol{u}^h, \boldsymbol{v}^h, \theta^h\}, \qquad \boldsymbol{u}^h = \sum_{A=1}^{n_b} \boldsymbol{u}_A N_A, \qquad \boldsymbol{v}^h = \sum_{A=1}^{n_b} \boldsymbol{v}_A N_A, \qquad \theta^h = \sum_{A=1}^{n_b} \theta_A N_A. \tag{15}$$

where N_A's are the basis functions, and n_b is the dimension of the discrete space. The NURBS basis functions with $\mathscr{C}^1$-continuity are used [13].

4. Distributed Computing

We describe the implementation details of the IGA code, cluster configuration, and weak performance scaling studies in the following subsections.

4.1. IGA Code Implementation

The models described by Eqs. (9) have highly nonlinear hysteretic behavior, strong thermo-mechanical coupling, and fourth-order differential terms in a space. These equations are not trivial to solve, especially in the 3D case, to solve on a regular workstation. We have used the distributed computing environment for the numerical simulations. In this work, we have applied the isogeometric analysis framework originally developed by Prof. T. Hughes' group at the Institute for Computational Engineering and Science, University of Texas at Austin, by adapting a publicly distributed NURBS code [18]. The code is written in the Fortran programming language (FORTRAN 90). We presented preliminary results for the 2D model using the IGA and serial processing in our paper [19]. Here, we present the numerical implementation of the 2D and 3D IGA models using the distributed computing environment. In this implementation, the IGA codes use a multiple instruction, multiple data (MIMD) architecture. The domain decomposition technique is employed in the distributed computing. The domain is decomposed spatially into smaller subdomains using a separate Matlab script as shown in Fig. 1. Major subroutines that are essential to the SMA thermo-mechanical physics in SMAs have been modified. One of the important considerations in solving fourth-order PDEs, with $\mathscr{C}^1$ continuity in the basis functions, is an efficient communication of additional information data on the boundaries between neighboring processors (shown with blue color lines in Fig. 1).

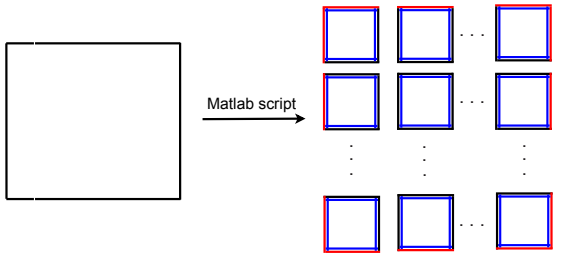

Fig. 1. (Color online) Schematic of domain decomposition used in the distributed computing environment. Additional data is passed (shown in blue color lines) along with the interprocessor communication data (shown in black color lines) and boundary condition data (shown in red color lines) to maintain $\mathscr{C}^1$ continuity of the basis function in the neighboring processors.

4.2. Cluster Configuration

All the simulations have been performed on the high-performance clusters of the Sharcnet computational facilities in Canada. More specifically, the simulations have been carried out on the Saw cluster (with each node having two 4-core Intel E5440 Quad Core Processors (2.83GH, 4 GB + 8GB FBD PC2-5300 Memory, and 120 GB of local storage) with InfiniBand 4X DDR running Linux CentOS release 6.3). The simulations have been performed utilizing full nodes and the performance data is collected.

4.3. Weak Scaling Performance Studies

We performed the weak scaling test with each MPI (message passing interface) task on a tile of spatial dimension 16 nm × 16 nm for the 2D model. The geometry is chosen such that it confirms the multiple of $8n$ processors, where node n is chosen as $n = 1, 2, 3, 4$ and 8 for the MPI studies. The serial study is performed on 1 processor. Each tile is discretized using two different meshes with (a) 128 (16384 elements, 33800 global and 18 local basis functions) and (b) 144 (20736 elements, 42632 global and 18 local basis functions) second order univariate NURBS basis functions in each direction. Figure 2 shows the performance data of the 2D model for 100 time steps using fixed time step and periodic boundary conditions with increasing number of processors (or MPI tasks). We access the parallelization performance using the efficiency η and speedup S defined as

$$\eta(n) = \frac{1}{n}\frac{T_{\mathrm{REF}}}{T_n}\frac{G_n}{G_{\mathrm{REF}}} \times 100, \qquad S(n) = \frac{T_{\mathrm{REF}}}{T_n}\frac{G_n}{G_{\mathrm{REF}}}, \tag{16}$$

where T_{REF} is the wall clock time on REF processing cores (in all the simulations REF = 1), and T_n is the wall clock time on n cores, G_{REF} and G_n are the numbers of global basis functions in the REF and n processing cores, respectively [20].

The plot in Fig. 2(a) indicates that the wall clock time is almost constant beyond 1 node (8 processors) which is also reflected in the efficiency plot in Fig. 2(b). The efficiency drops significantly to around 55 % and 45 % using mesh tile with 128, and 144 basis functions, respectively. The steepest drop is due to several reduction operations used in the code which is evident from Fig. 3 (b). Fig.2(c) shows the speedup for two different meshes. Fig. 3(a) shows the breakdown of the computational and MPI communication time using mesh with 128 basis functions solved on two nodes with 8 processors each. The code spends 60.7 % time in MPI calls and Fig. 3(b) indicates the reason for stabilizing the efficiency around 55 % for mesh with 128 NURBS basis functions. The MPI_ALLREDUCE calls consume 83.36 % of MPI time. As the MPI_ALLREDUCE is a call blocking communication, all the processors wait for the statement to execute, thus leading to active waiting. In the overall simulation, the maximum workload imbalance of 10.9 s has been observed. There is an opportunity to improve the computational efficiency by changing the code implementation, which is being investigated. We note that the poor scaling found in our results has nothing to do with the IGA technology itself, but is a result of our particular implementation. Excellent scalings for IGA algorithms have been achieved by using the concept of Bézier extraction [21] or PETSc-based implementations (see PetIGA [22]).

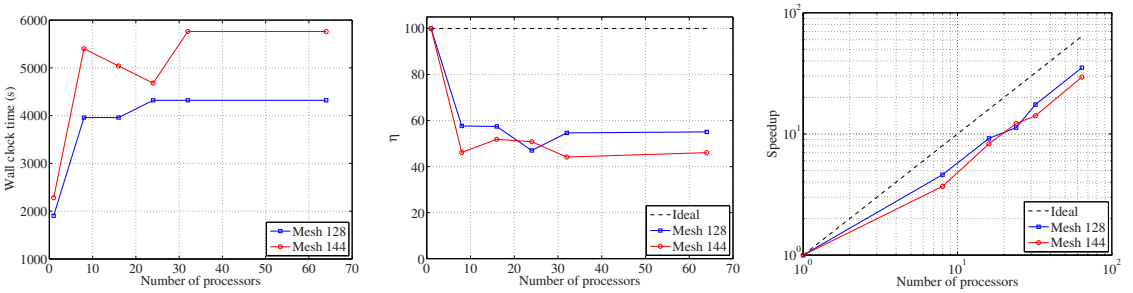

(a) Wall clock time (b) Efficiency η (c) Speedup

Fig. 2. Weak scaling performance data for the 2D model on the Sharcnet's Saw cluster using mesh tiles with 128 and 144 NURBS basis functions (processors (node) used during the simulations are 8(1), 16(2), 24(3), 32(4), and 64(5)).

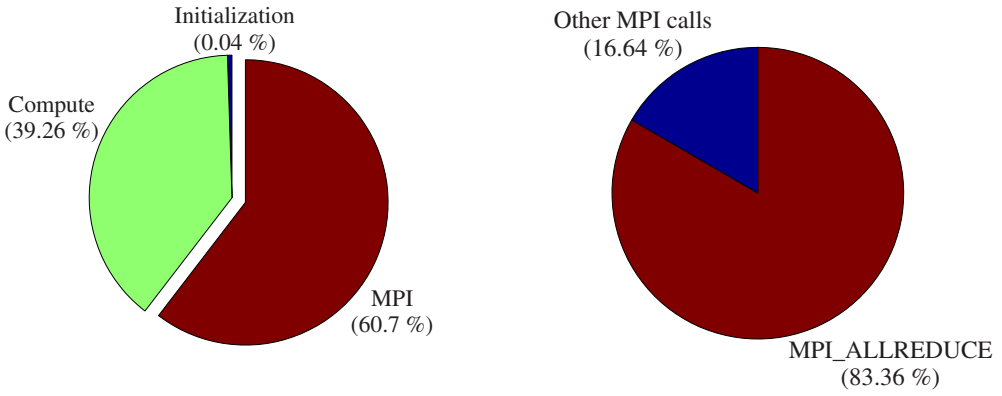

(a) (b)

Fig. 3. (Color online) Overall percentage breakdown of (a) different times (initialization, computation and MPI), and (b) MPI time during weak scaling performance simulation using 16 processors on two full nodes with mesh tile having 128 NURBS basis functions.

5. Numerical Simulations and Results

We present results of numerical simulations using the developed models based on the IGA. The numerical simulations have been performed on the domain Ω^d (with d = 2,3). The IGA is capable of representing any arbitrary complex geometry; however as a proof of concept, we use simple geometries in the 2D and 3D models. Here we mainly focus on the cubic-to-tetragonal phase transformations in the $Fe_{70}Pd_{30}$ material, which is gaining more attention due to its thermal, mechanical, and magnetic coupling and biocompatibile properties [23, 24, 25]. The material parameters for $Fe_{70}Pd_{30}$ can be found in [8, 11], and [26]. For serial processing, we have recently presented the mesh convergence study results for the 2D model in [19]. Here, we solve the 2D and 3D models in the distributed computing environment under different initial and boundary conditions. The NURBS can be used to model and discretize a complex geometry, however all the simulations here have been performed by employing a uniform mesh composed of $\mathscr{C}^1$-continuous quadratic elements.

5.1. 2D Model

The 2D simulations have been conducted on a square domain with 100 nm side. The microstructure is evolved starting from an initial displacement seed (in dimensionless unit) in the centre of the domain (x_c, y_c) defined as

$$u_{1_0} = \exp^{-(x-x_c)^2\times 10^3} \times \exp^{-(y-y_c)^2\times 10^3} \times 10^{-3}, \qquad u_{2_0} = -u_{1_0},$$

and initial temperature $\theta_0 = 250$ K. All the sides of the domain are constrained in the structural degrees of freedom. The simulations have been performed on 16 processors (with 4 processors in the X and Y directions). The microstructure has been allowed to evolve for sufficiently long time by minimizing the energy till it no longer evolves. Fig. 4(a) shows the stabilized microstructure (deviatoric strain e_2). The two variants of martensite (shown in red and blue colors) are self-accommodated by aligning domain walls diagonally. The self-accommodation of martensites is in agreement with the model results in the literature (e.g. [9]).

5.2. 3D Model

The 3D simulations have been carried out under the fully periodic boundary conditions on a cube with 80 nm side. The microstructure has been evolved starting from random initial conditions and initial temperature $\theta_0 = 240$ K. The simulations have been performed on 64 processors (4 processors in each direction). Fig. 4(b) shows the microstructure (deviatoric strain e_2) at 1400 time step. The simulation results show that the accommodated martensitic microstructures are in agreement with known results obtained with other models [27, 26, 10]. We have used the adaptive time stepping scheme during the microstructure evolution [11, 19]. As mentioned earlier, the distributed computing code uses several reduction operations, and it is being modified to improve the characteristic performance.

6. Conclusions

The coupled non-linear thermo-mechanical models for SMAs have been developed by using the Ginzburg-Landau theory and variational framework. The developed models have been numerically solved based on the IGA. It has been shown on several examples that the microstructure evolution is in agreement with known results from the literature. The weak scaling performance studies indicate a pronounced decrease in the efficiency above 8 MPI tasks due to increased communication overhead in the 2D model. These studies demonstrate current computational challenges and open a way for future improvements.

Acknowledgments

RD, RM, and JZ have been supported by the NSERC and CRC program (RM), Canada. This work was made possible with the facilities of the Shared Hierarchical Academic Research Computing Network SHARCNET: www.sharcnet.ca) and Compute/Calcul Canada.

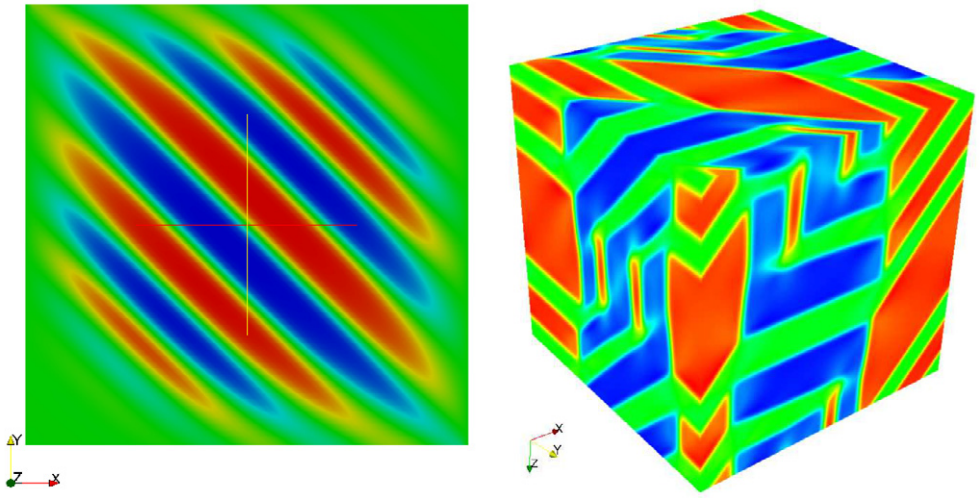

(a) (b)

Fig. 4. (Color online) Evolved microstructures (deviatoric strain e_2) in FePd specimens using the developed (a) 2D , and (b) 3D phase-field models at 3000, and 1400 time step, respectively.

References

[1] K. Otsuka, C. Wayman, Shape memory materials, Cambridge University Press, New York, 1998.
[2] E. Patoor, D. Lagoudas, P. Entchev, L. Brinson, X. Gao, Shape memory alloys, Part I: General properties and modeling of single crystals, Mechanics of Materials 38 (5) (2006) 391–429.
[3] D. Lagoudas, L. Brinson, E. Patoor, Shape memory alloys, Part II: Modeling of polycrystals, Mech. Mater. 38 (5-6) (2006) 430–462.
[4] A. Khandelwal, V. Buravalla, Models for Shape Memory Alloy Behavior: An overview of modelling approaches, International Journal of Structural Changes in Solids - Mechanics and Applications 1 (1) (2009) 111–148.
[5] F. Falk, Model free energy, mechanics, and thermodynamics of shape memory alloys, Acta Metallurgica 28 (12) (1980) 1773–1780.
[6] R. Melnik, A. Roberts, K. A. Thomas, Computing dynamics of Copper-based SMA via center manifold reduction models, Computational Material Science 18 (2000) 255–268.
[7] T. Lookman, S. R. Shenoy, K. Rasmussen, A. Saxena, A. R. Bishop, Ferroelastic dynamics and strain compatibility, Phys. Rev. B Condens. Matter. Mater. Phys. 67 (2) (2003) 24114.
[8] R. Ahluwalia, T. Lookman, A. Saxena, Dynamic Strain Loading of Cubic to Tetragonal Martensites, MRS Bull. 54 (2006) 2109–2120.
[9] M. Bouville, R. Ahluwalia, Microstructure and Mechanical Properties of Constrained Shape Memory Alloy Nanograins and Nanowires, Acta Mater. 56 (14) (2008) 3558–3567.
[10] A. Idesman, J. Cho, V. Levitas, Finite Element Modeling of Dynamics of Martensitic Phase Transitions, Appl. Phys. Lett. 93 (4) (2008) 043102.
[11] R. Dhote, R. Melnik, J. Zu, Dynamic thermo-mechanical coupling and size effects in finite shape memory alloy nanostructures, Computational Materials Science 63 (2012) 105–117.
[12] L. Wang, R. Melnik, Modifying Macroscale Variant Combinations in a Two-Dimensional Structure using Mechanical Loadings during Thermally Induced Transformation, Mater. Sci. Eng. A Struct. Mater. 481-482 (2008) 190–193.
[13] C. Austin, T. Hughes, Y. Bazilevs, Isogeometric Analysis: Toward Integration of CAD and FEA, John Wiley & Sons., 2009.
[14] H. Gomez, T. J. Hughes, X. Nogueira, V. M. Calo, Isogeometric analysis of the isothermal Navier-Strokes-Korteweg equations, Computer Methods in Applied Mechanics and Engineering 199 (25-28) (2010) 1828–1840.
[15] H. Gomez, V. Calo, Y. Bazilevs, T. Hughes, Isogeometric analysis of the Cahn-Hillard phase-field model, Computer Methods in Applied Mechanics and Engineering 197 (49-50) (2008) 4333–4352.
[16] R. Dhote, M. Fabrizio, R. Melnik, J. Zu, Hysteresis Phenomena in Shape Memory Alloys by Non-Isothermal Ginzburg-Landau Models, Communications in Nonlinear Science and Numerical Simulation, doi: http://dx.doi.org/10.1016/j.cnsns.2013.01.015.
[17] C. Carstensen, On the computational of crystalline microstructure, Acta Numerica 5 (1996) 191256.
[18] NURBS code, http://users/ices.utexas.edu/~evans/isogeometric.zip.
[19] R. Dhote, H. Gomez, R. Melnik, J. Zu, Phase field dynamic modelling of shape memory alloys based on isogeometric analysis, Advances in Science and Technology 78 (2013) 63–68.
[20] D. Valdez-Balderas, J. M. Domínguez, B. D. Rogers, A. J. Crespo, Towards accelerating smoothed particle hydrodynamics simulations for free-surface flows on multi-GPU clusters, Journal of Parallel and Distributed Computing (article in press-doi:http://dx.doi.org/10.1016/j.jpdc.2012.07.010.
[21] M. A. Scott, M. J. Borden, C. V. Verhoosel, T. W. Sederberg, T. J. R. Hughes, Isogeometric finite element data structures based on bézier extraction of t-splines, International Journal for Numerical Methods in Engineering 88 (2) (2011) 126–156.

[22] PetIGA, https://bitbucket.org/dalcinl/petiga/.
[23] Y. Ma, M. Zink, S. Mayr, Biocompatibility of single crystalline FePd ferromagnetic shape memory films, Applied Physics Letters 96 (2010) 213703.
[24] K. Žužek Rožman, D. Pečko, S. Šturm, U. Maver, P. Nadrah, M. Bele, S. Kobe, Electrochemical synthesis and characterization of $Fe_{70}Pd_{30}$ nanotubes for drug-delivery applications, Materials Chemistry and Physics 133 (1) (2012) 218–224.
[25] C. Bechtold, A. Lotnyk, B. Erkartal, L. Kienle, E. Quandt, Structural Characterization of Sputtered $Fe_{70}Pd_{30}$ Thin Films During Ex Situ and In Situ TEM Heating, Advanced Engineering Materials 14 (8) (2012) 716–723.
[26] R. Ahluwalia, T. Lookman, A. Saxena, S. Shenoy, Pattern formation in ferroelastic transitions, Phase Transitions 77 (5-7) (2004) 457–467.
[27] A. Jacobs, S. Curnoe, R. Desai, Simulations of cubic-tetragonal ferroelastics, Physical Review B 68 (22) (2003) 1–7.